Materials & Design 259 (2025) 114847

Contents lists available at ScienceDirect

Materials & Design

journal homepage: www.elsevier.com/locate/matdes

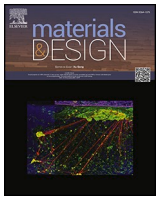

# Precipitation distribution in mechanically alloyed Al-Cu-Li powders processed via friction consolidation

Chang Yin-Cheng Chan [a,*], Uceu F.H.R. Suhuddin [a], Emad Maawad [b], Mark T. Mordridge [c], Benjamin Klusemann [a,d]

[a] Helmholtz-Zentrum Hereon, Institute of Material and Process Design, Solid State Materials Processing, Max-Planck-Str. 1, 21502 Geesthacht, Germany
[b] Helmholtz-Zentrum Hereon, Institute of Materials Physics, X-Ray Diffraction with Synchrotron Radiation, Max-Planck-Str. 1, 21502 Geesthacht, Germany
[c] Helmholtz-Zentrum Hereon, Institute of Materials Physics, Metal Physics, Max-Planck-Str. 1, 21502 Geesthacht, Germany
[d] Leuphana University of Lüneburg, Institute for Production Technology and Systems, Universitätsallee 1, 21335 Lüneburg, Germany

ARTICLE INFO

*Keywords:*
Aluminum alloys
Friction consolidation
Mechanical alloying
Precipitation strengthening
High-energy X-ray diffraction

ABSTRACT

Friction consolidation (FC) was deployed to illustrate the mechanical alloying effect of Al-Cu, Al-Li, and pure Cu powder through phase transformation behavior. A progressive material flow from the periphery to the center of the FC die was witnessed, along with expansion perpendicular to the direction of rotation, indicating various degrees of alloying. Two types of precipitate, $\delta'(Al_3Li)$ and $T_1(Al_2CuLi)$, were identified, exhibiting different distributions, attributed to variations in Cu content and thermo-mechanical processing. Mechanical tests showed slight anisotropic mechanical properties of the consolidated samples. By estimating the precipitate strengthening effect using physical models, the strengthening of $\delta'$ was found to be more prominent than that of $T_1$, which might be more prone to strain localization. Overall, the results demonstrate the feasibility of FC in processing Al-Cu-Li alloys and serve as basis for further improvements in the final product through the addition of minor alloying elements, demonstrating an energy-efficient manufacturing process for such alloys.

## 1. Introduction

Al-Cu-Li alloys have garnered significant interest in aerospace applications over the past decades owing to their excellent combination of properties, including low density, high specific strength, excellent corrosion resistance, and fatigue crack resistance [1–3]. The enhancement of these properties is attributed to the precipitate strengthening effect during the aging process, involving precipitates such as spherical $\delta'(Al_3Li)$, plate-like $\theta'(Al_2Cu)$, and plate-like $T_1(Al_2CuLi)$, with $T_1$ being considered the most significant strengthening precipitate [4]. High Li content, exceeding 2 wt%, was added in the early development of Al-Li alloys to improve weight reduction and increase the elastic modulus. But these alloys experience low ductility due to the main strengthening precipitate $\delta'$ being prone to plane slip under plastic deformation [5]. Furthermore, high Li content Al-Li alloys also suffer from high anisotropy of mechanical properties and low fracture toughness [1]. As a result, in the current third generation of Al-Li alloys, the Li content is reduced to below 2 wt% with the addition of heavy or precious elements such as Mg, Ag, Mn, Zn and Zr to optimize and reach the demanded properties in terms of grain refinement, corrosion resistance, and thermal stability [6–8].

Due to the high reactivity of Li, the casting of Al-Li alloys requires special treatment to ensure good ingot quality regarding the uniform phase distribution and minimal Li volatilization. Several attempts, such as the usage of an Al-Li master alloy, inert gas flushing, and vacuum melting with inert gas (Ar), have been reported, with the latter being seen as a promising route to manufacture high-quality ingot materials [9,10]. Recently, Li et al. [11] presented a low Li content (~1 wt%) Al-Li alloy with fine grains, low porosity, and no component segregation, manufactured through ultrasonic treatment coupled with squeeze casting. Liu et al. [12] reported a high Li content (~4 wt%) Al-Li alloy ingot with uniform phase distribution and no segregation through a two-step casting, where a dense pure-Al block was placed atop pure Li granulate. Apart from melt-based processing methods that are manufactured under or at least close to equilibrium thermodynamic conditions, solid-state processing methods, such as equal channel angular pressing (ECAP), high-pressure torsion (HPT) and friction stir additive manufacturing (FSAM), have been carried out to investigate novel alloys under non-

* Corresponding author.
*E-mail address:* chang.chan@hereon.de (C.Y.-C. Chan).

https://doi.org/10.1016/j.matdes.2025.114847
Received 22 April 2025; Received in revised form 26 June 2025; Accepted 26 September 2025
Available online 28 September 2025

equilibrium conditions [13–15]. Munoz-Morris and Morris [13] achieved fine precipitates within an Al-Cu-Li alloy by ECAP, simultaneously improving strength and elongation. Dong et al. [14] developed an ultrafine grain structure via HPT in an Al-Cu-Li alloy and the subsequent aging procedure proposed that clustering strengthening contributes to the high strength. Shen et al. [15] obtained excellent mechanical properties in the effective additive zone in FSAM, indicating the potential of solid-state additive manufacturing of Al-Cu-Li alloys. Nonetheless, all studies kept the Li content below 2 wt%.

Friction consolidation (FC), a friction-based solid-state processing technology, has attracted attention in the past decade due to its ability to promote diffusion in metals through high shear strain, leading to the discovery of metastable states [16]. Research on FC has focused on recycling and alloying, with several studies reporting the successful recycling of Al machining chips [17–20]. Li et al. [17] identified two distinct FC processing stages, namely compaction and consolidation, differentiated by the onset of the solid bonding. Although the process region in FC is asymmetric in the perpendicular direction to the die-feedstock interface, process parameter optimization can minimize this inhomogeneity, though not eliminate it entirely [18,19]. Latif et al. [19] proposed a multi-step approach that achieved more uniform grain size and mechanical properties by balancing the plastic deformation. Ingarao et al. [20] compared the life cycle assessment (LCA) of single- and multi-step FC with the remelting route, revealing that the ideal multi-step FC considerably reduces the environmental impact while preserving an adequate homogeneity. Additionally, FC enables the synthesis of various powders, such as oxide dispersion strengthened (ODS) steel [21–23], semiconducting $Bi_2Te_3$ [24], and metal matrix composites (MMCs) [25,26], with enhanced performance. Zhang et al. [22] proposed FC as an alternative pathway for manufacturing ODS steel, demonstrating a tenfold increase in the density of nano-oxides, which is beneficial for both radiation resistance and high-temperature creep strength, due to shear deformation-induced fragmentation of the oxide layer in the powder precursor. Wang et al. [23] further illustrated the concept by combining the FC puck with friction extrusion (FE) to produce an ODS steel rod under low process temperatures, restraining grain coarsening. Li et al. [25] utilized FC to homogeneously distribute $TiB_2$ in Al to form MMC and reported significant improvements in ultimate tensile strength (UTS), Young's modulus, and wear resistance compared to other Al MMCs. However, it suffered a critical ductility reduction. Furthermore, Cu-Ni and Cu-Nb mixed powder with complete and immiscible solubility, respectively, have been deployed to research the onset of alloying in FC and indicated the preferential diffusion of lower-strength Cu into Ni or Nb [27,28]. In the Cu-Ni system, shear deformation first recrystallized and infiltrated Cu into Ni-Ni high-angle grain boundaries (HAGBs), and subsequently accumulation in Ni particles initiates the onset of alloying to reduce the strain gradient in the lattice [27]. Komarasamy et al. [28] observed supersaturation of Nb in Cu, exceeding its equilibrium solubility, attributed to forced supersaturated solubility. However, similar works for Al-based FC processes have not been fully explored.

In this study, 2 wt% Li, considered as high Li content in the current generation of Al-Cu-Li alloys, is chosen to demonstrate the feasibility of the mechanical alloying effect of Al-Cu-Li alloys from powder feedstock via FC through phase transformation. The distribution of precipitates and their formation mechanisms are correlated with temperature history and the extent of shear deformation. Further heat treatment is deployed to the selected sample to reveal the artificial aging response.

## 2. Materials and methods

### 2.1. Materials

Commercially available powders, including AlCu4.5 wt% (gas-atomized with a particle size smaller than 63 μm, Sindlhauser), AlLi20 wt% (< 50 μm, American elements) and pure Cu (E.MERCK KG) powders (< 90 μm) were used as-received as feedstock material, as shown in Fig. 1. The AlCu, AlLi and pure Cu powders show a spherical, flake and dendritic morphology, respectively. A phase segregation at grain boundaries is present in the AlCu powder, which is typically observed in gas-atomized powder [29]. Moreover, the dendritic morphology is the typical morphology of pure Cu manufactured via the electrolysis process. An alloy with a nominal composition of AlCu6Li2 (wt%) with a total of 65 g was weighed using a high-precision scale (Kern PNS 3000–2), sealed in a plastic container, and blended in a laboratory blender (MIXOMAT mini, FUCHS) for 15 minutes with a rotation speed of 33 rpm. A visual inspection was conducted to ensure complete blending. The blended powder was then compacted using a hydraulic press (P/O/WEBER PWE-E) into the feedstock container under 100 kN. Storage and handling materials were conducted inside an Ar-filled glovebox to protect against oxidation. The feedstock container was then assembled into the dedicated FE machine FE100 (Bond Technologies) shortly before the friction consolidation (FC) process to minimize contact with the ambient environment and potential oxidation.

The FC process is illustrated in Fig. 2. A non-consumable one scroll die from H13 steel with a 50 mm diameter and a feedstock container machined from AISI 4400 steel with an inner diameter of 50 mm were used in the present study. The process temperatures were recorded through a K-type thermocouple mounted at a radius of 16.5 mm and 1 mm below the die face. The FC process starts with rotating the feedstock container, followed by plunging the non-rotating die into the feedstock container. A low-force approach with 200 rpm and a limited force of 50 kN was performed to a plunged depth of 1 mm into the compacted blended powder to avoid damage to the tooling and the machine due to torque overload. Based on preliminary experiments, the actual FC process was conducted under forces at 200 kN with a constant rotational speed of 200 rpm. Four different processing times, 5, 20, 40 and 60 s, were used to unveil the effect of processing time and the material flow. Additionally, artificial aging at 175 °C for 20 h, using a NA 120/85L furnace (Nabertherm), was conducted on the 20 s sample to investigate its precipitation evolution.

### 2.2. Microstructural characterization

Friction consolidated (FCed) samples were cross-sectioned,

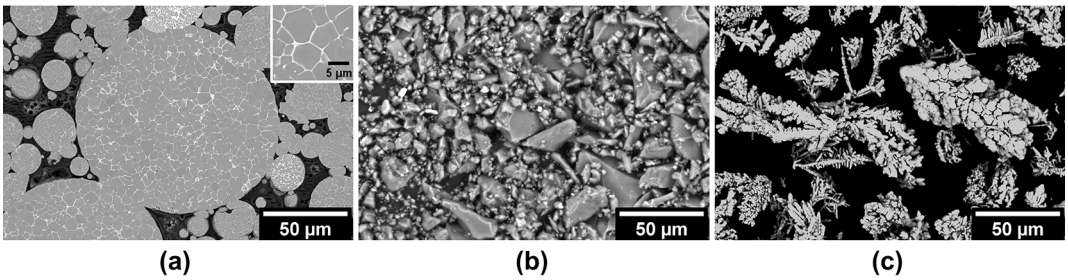


**Fig. 1.** Backscattered electron (BSE) images of base materials, including (a) AlCu4.5 powder with an inset highlighting the Cu segregation at grain boundaries, (b) AlLi20 powder and (c) pure Cu powder.

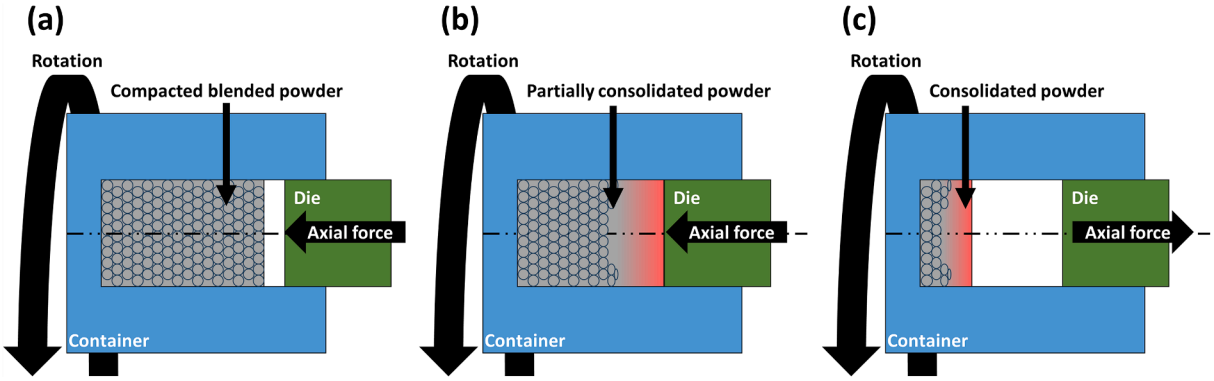


**Fig. 2.** Schematic illustration of friction consolidation process using powder feedstock. (a) The blended powder is initially compacted within a container. (b) The FC process continuously consolidates the blended powder through rotational motion and compressive force. (c) The process finishes with the retraction of the die, resulting in fully consolidated powder.

embedded, ground, and polished, following standard metallographic preparation procedures. Samples for optical microscopy were etched with Barker etchant with 15 V for 90 s and observed under a Keyence VHX-6000 digital microscope. Further analysis of the FCed samples and the blended powders were conducted using a Thermo Fisher Quanta 650 field-emission gun scanning electron microscope (FEG-SEM) equipped with EDAX Octane Elect energy-dispersive X-ray spectroscopy (EDX). In specific regions of the sample processed for 20 s, additional transmission electron microscope (TEM) observations were conducted to identify the precipitates. TEM lamellae were prepared with a gallium focused ion beam (FIB) in a Thermo Fisher Nova Nanolab 200 FIB/SEM. Both STEM and TEM inspection were undertaken in a Thermo Fisher Talos F200i TEM, equipped with dual Bruker X-Flash 6 EDS detectors.

Phases and precipitates within the FCed sample were identified using high-energy X-ray diffraction (HEXRD) at the beamline P07, partially operated by the Helmholtz-Zentrum Hereon at the synchrotron source PETRA III of the Deutsches Elektronen Synchrotron (DESY) in Hamburg, Germany. A monochromatic X-ray beam with an energy of 103.8 keV (wavelength: 0.1194 Å) and beam size of 0.5 mm x 0.5 mm was used for a two-dimensional scan with a step size of 0.5 mm, providing map characterization. The total scanning distance was 5 mm perpendicular to the die-feedstock interface and covered the complete sample in radial direction. Full Debye-Scherrer rings were acquired in transmission mode via a two-dimensional Perkin-Elmer XRD1621 detector with a maximum $2\theta$ angle of ~10°. The raw data was azimuthally integrated over 360° using the Fit2D software [30] to obtain one-dimensional diffraction patterns. Qualitative phase analysis was achieved by indexing the diffraction peaks according to Powder Diffraction Files (PDFs) of relevant phases from the International Center for Diffraction Data (ICDD) database. Estimation of the quantitative phase volume fraction was

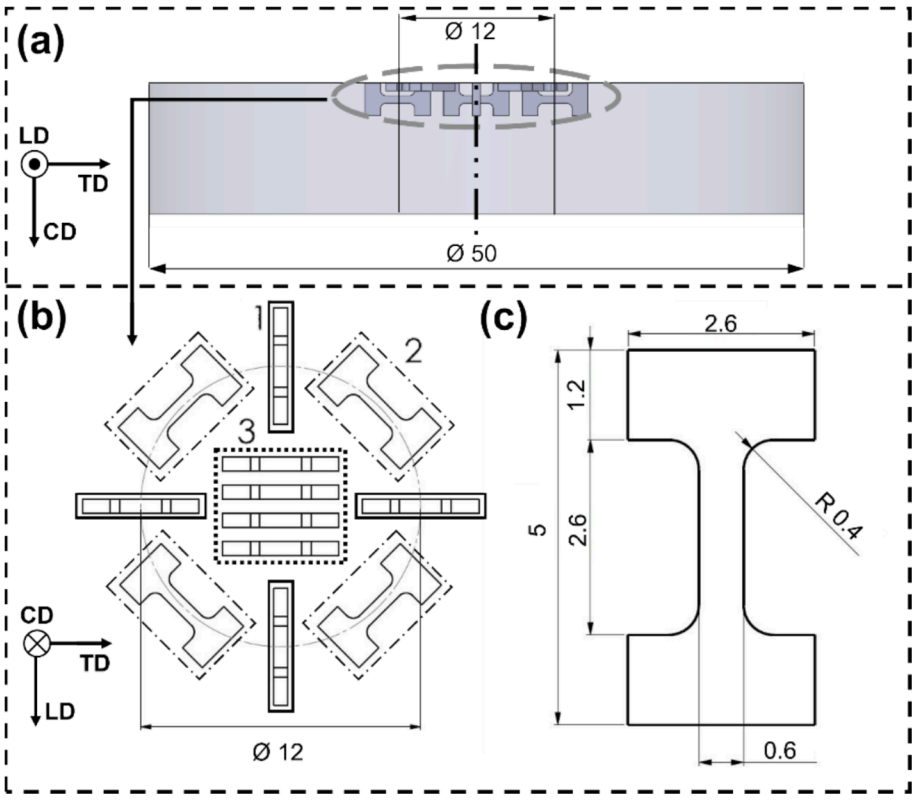


**Fig. 3.** Microflat tensile specimens with 0.6 mm thickness are extracted from the top surface of the FCed sample, close to the die-feedstock interface (a). The detailed orientation and dimensions of the specimens are summarized in (b) and (c), respectively. All dimensions are in mm.

conducted through Rietveld refinement of the integrated diffraction patterns using the Materials Analysis Using Diffraction (MAUD) software [31].

### 2.3. Mechanical testing

Mechanical properties were assessed by microhardness and micro-tensile testing. Microhardness measurements were performed utilizing a Struers Durascan 70 G5 machine with a load of 0.2 kgf and a dwell time of 15 s. A two-dimensional microhardness map was generated with a grid size of 0.5 mm covering half of the FCed sample, assuming symmetry along the rotational axis. Micro-tensile tests were conducted on the 20 s processed sample, in as-FCed and artificially aged state, via a Deben Microtest MT5000 at a rate of 0.1 mm/min. Based on microstructure characteristics, the microflat tensile specimens were separated into three groups, including two different orientations at a radius of 6 mm (marked as 12 mm in diameter in Fig. 3) as well as from the center of the FCed samples. All the specimens were extracted using electrical discharge machining (EDM) near the die-feedstock interface, with only the rough surface marks from the FC die removed to achieve a smooth surface. In each group, three specimens were tested to ensure statistical reliability. The dimensions and the detailed positioning of the samples are summarized in Fig. 3. The consolidation direction (CD), transverse direction (TD) and longitudinal direction (LD) are also given to illustrate the orientation.

## 3. Results

### 3.1. Blended powder

The microstructural features of the blended powder are illustrated in Fig. 4. The low magnification backscatter electron (BSE) image in Fig. 4 (a) reveals bright (indicated by red arrows) and dark (indicated by light blue arrows) particles homogeneously distributed throughout the sample. Energy-dispersive X-ray spectroscopy (EDX) analysis identifies the bright particles as pure Cu, while the dark particles show a high oxygen content and a depletion of Al, see Fig. 4(b). Given that standard sample preparation involves exposure to water and the high reactivity of AlLi powder, it can be assumed that the dark particles are initially AlLi powder and oxidized during sample preparation. Nevertheless, the uniform distribution of both particles confirms the homogeneity of the blended powder and ensures that each powder does not aggregate.

### 3.2. Macro/microstructure of the friction consolidated samples

The macrostructure of the processed samples is summarized in Fig. 5. Two distinct regions can be identified based on porosity or undissolved raw powder density, see the white dashed line in Fig. 5. Below this separation line, a high number of defects, characterized by porosity after powder compaction, are visible, indicating the powder in this region experienced minimal to no shear deformation, classifying it as the non-consolidated region. The region above is characterized as the consolidated region. Because the consolidated region is in the vicinity of the die-feedstock interface, it experiences higher shear deformation and frictional heat introduced by the consolidation die, with these effects diminishing toward the bottom of the consolidated region. The combination of intensive shear deformation and exposure to high heat input in the consolidated region likely triggered dynamic recrystallization, leading to defect elimination and grain refinement. Since the macrostructural features are nearly symmetric along the rotational axis, the following analyses are presented for only half of each sample.

The 20 s friction consolidated (FCed) sample, representing an intermediate stage in the processing time and containing all key macrostructural features, is used as a basis for discussing the macrostructure after FC, as detailed below:

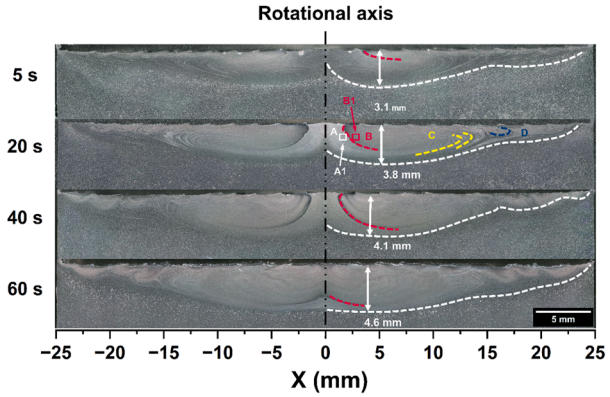


**Fig. 5.** Macrograph of friction consolidated (FCed) samples at different processing times, i.e. 5, 20, 40 and 60 s from top to bottom. The depth of the consolidated region is measured for each sample. Four different features are marked with different colors (A-D).

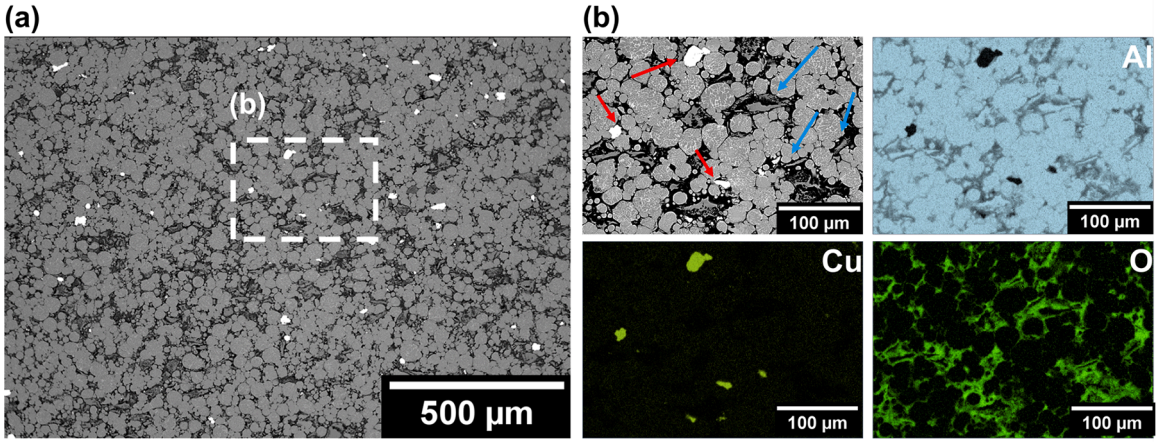


**Fig. 4.** BSE image of the blended powder at low (a) and high (b) magnification. Pure Cu and AlLi powders are indicated by red and light blue arrows, respectively. The corresponding EDX elemental maps for Al, Cu and O are also present. (For interpretation of the references to colour in this figure legend, the reader is referred to the web version of this article.)

(1) At the center of the consolidated region, denoted as region A in Fig. 5, a horizontally layered material flow pattern is observed, suggesting that the material was mainly pressed down by the die with only slight shear deformation, analogues to the onion rings concept present in Friction Stir Welding (FSW) [32], as shown in Fig. 6(a). Notably, no evidence of inward material flow is present, indicating that this region has not been affected by the scroll feature-induced flow.
(2) Moving outward from the center, the red curved line marks a boundary to another distinct region, denoted as region B, tilting from the horizontal. This boundary represents the separation between region B, which exhibits inward material flow introduced by the scroll feature at the die-feedstock interface, and region A, which is influenced by pressed-down material flow. Region B exhibits a bowl-shaped structure, which is referred to as the recrystallization region, as described by Buffa et al. [18].
(3) Further outward, indicated by the yellow lines, this region is denoted as region C, which is characterized by material flow drawn toward the center by the scroll feature at the die-feedstock interface and outward material flow from the center at the bottom of the consolidated zone, following the law of conservation of mass.
(4) Near the edge of the FCed samples, turbulent material flow, marked by the blue line and denoted as region D, becomes evident. As the radius increases, the corresponding centrifugal force also increases, counteracting the inward material flow introduced by the scroll die. As a result, the material in this region undergoes primarily tangential movement, with minimal radial movement.

The vertical growth of the consolidated region correlates clearly with increased processing time, which is associated with the propagation of heat generated at the interface as well as deeper propagation of shear deformation into the FCed sample. The central horizontally layered feature is gradually replaced by region B as processing time increases, indicated by the shifting red curves, reflecting changes in material flow during FC. On the other hand, the horizontal width of the process zone lacks a distinct boundary accompanying the existence of the outer vortex, making the boundary in the horizontal direction vague. Region C remains at about 60 % of the maximum radius, suggesting limited inward material flow under these processing conditions. This observation aligns with the "dead metal" zone concept, deduced by Li et al. [33]. Since the boundary of the inward material flow expands and replaces the horizontally layered feature at the center with increased processing time, it is crucial to investigate the differences across the transition boundary between regions A and B to reveal the transformation mechanism during FC. For clarity, the side closer to the rotational axis and the side away from the rotational axis will be denoted as positions A1 and B1, respectively, see Fig. 5.

The BSE images along with the Cu EDX mapping at the center of the FCed sample, as well as across the transition boundary between regions A and B (marked by the red curve), are summarized in Fig. 6. At the center, Fig. 6(a-b), secondary phases align horizontally in a layered structure, as highlighted by Cu in the EDX mapping. Given the distinct Cu composition in the raw powder, the layered Cu distribution suggests that some minor shear deformation has been introduced but mechanical alloying is incomplete in this region. In Fig. 6(c-d), the transition boundary shows a high Cu content, suggesting that instead of forming a complete supersaturated solid solution (*SSSS*), some Cu is pushed toward the center by the material flow. According to the high-temperature Al-Cu-Li ternary phase diagram [34], the solubility of Cu with 2 wt% Li is less than 4.5 wt%, further confirming that a complete *SSSS* is not formed during the process. Secondary phases nucleate at grain boundaries on both sides of the transition boundary are observed in BSE images, see Fig. 6(e, g), with a higher density on the side closer to the rotational axis (position A1), as shown in Fig. 6(e-f). Since the transition boundary separates the inward material flow, more severe plastic deformation and mechanical alloying effects are expected on the side away from the rotational axis (position B1), as shown in Fig. 6(g-h), resulting in lower secondary phases density.

EDX is unable to distinguish different phases due to the presence of Li, therefore, further phase identification was performed by HEXRD, and the selected results at positions A1 and B1 are summarized in Fig. 7. The compacted powder is denoted as the base material (BM), showing predominant Al, Cu, $\delta(AlLi)$ and $\theta(Al_2Cu)$ reflections from the raw powders. In the FCed sample, the presence of $T_1$ diffraction peaks at both positions A1 and B1, along with the prominent Al peaks and the absence of Cu, $\theta$ and $\delta$ peaks, confirms the occurrence of mechanical alloying during FC. Furthermore, since the $T_1$ precipitate has been reported to nucleate both intragranularly and intergranularly [35], and the absence of the $\theta$ and $\delta$ peaks, the secondary phases observed in the BSE images are likely $T_1$. After artificial aging, an additional $\delta'$ phase was observed, indicating the formation of a *SSSS* in the as-FCed state.

The volume fraction of precipitates was quantified via Rietveld refinement and the different distributions are shown in Fig. 8(a-b). The artificially aged sample is 1.5 mm off center due to the sample cutting, therefore, all the following mapping starts from 1.5 to 25 mm. However, the transition boundary marked by the red curve in Fig. 5 is preserved. The higher volume fraction of $T_1$ precipitate lies at the center of region B as well as along a line at the bottom of region A in both as-FCed and

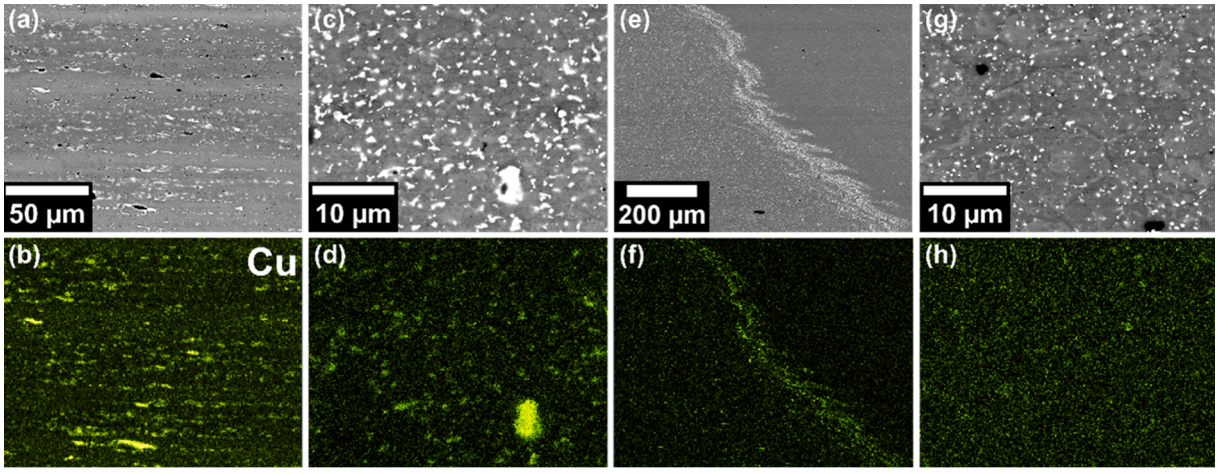


**Fig. 6.** BSE images and the corresponding Cu EDX mapping at the FCed sample center (a-b) as well as across the boundary of regions A and B, in which on the side close to the rotational axis denoted as A1 (c-d), the transition boundary center (e-f) and on the side away from the rotational axis denoted as B1 (g-h), see also Fig. 5.

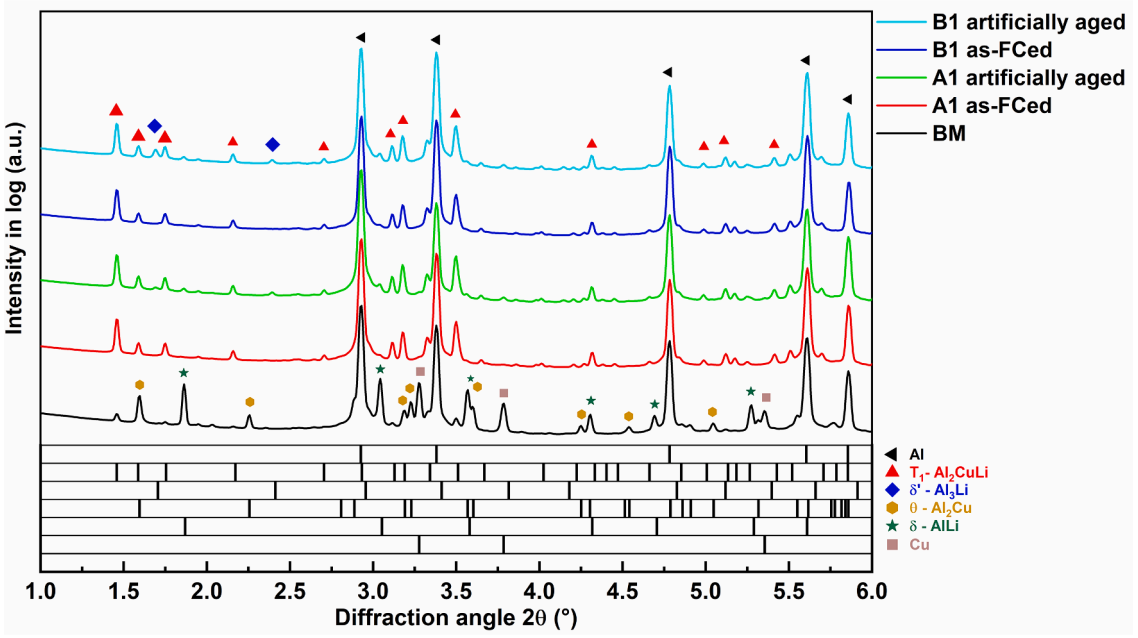


**Fig. 7.** HEXRD diffractograms of position A1 and position B1, see Fig. 5, in the as-FCed state as well as in artificially aged state, with addition of base material.

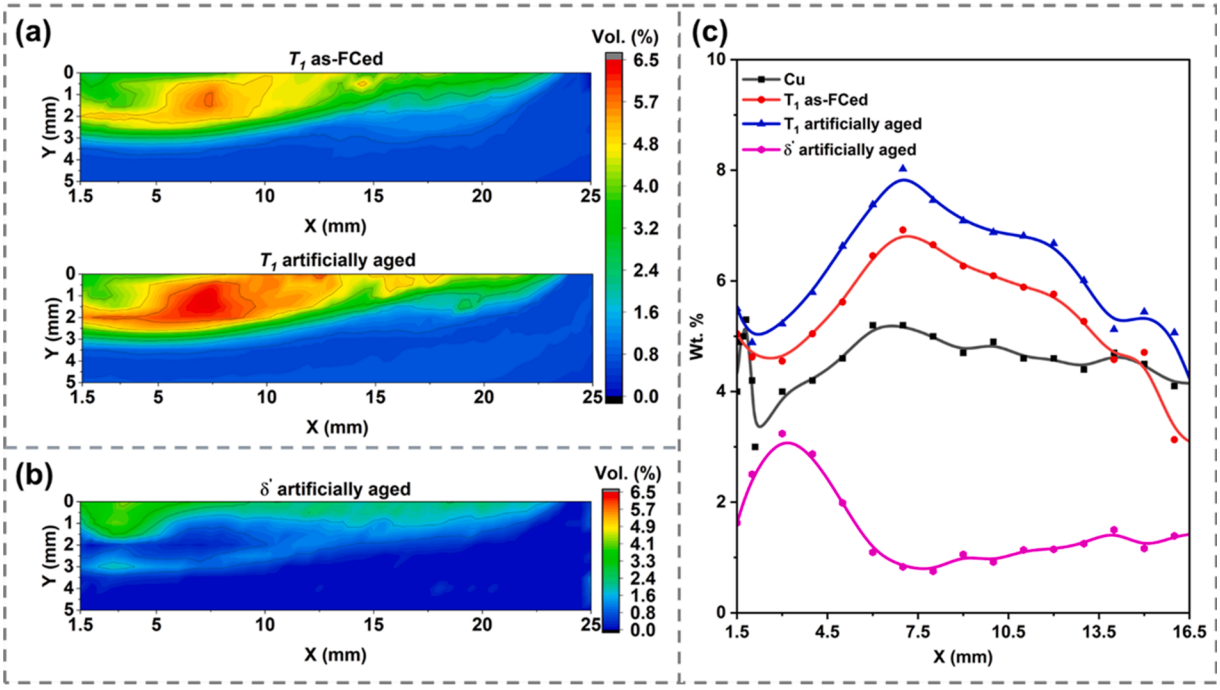


**Fig. 8.** Precipitate distribution of (a) $T_1$ in the as-FCed state (above) and after artificial aging (middle) and (b) $\delta'$ after artificial aging. (c) The weight fraction of $T_1$ and $\delta'$ at y = 1 mm at different radial distances, along with the Cu wt % from EDX.

artificially aged samples. The distribution of $T_1$ precipitate remained unaltered after artificial aging, but the volume fraction increased. For the $\delta'$ precipitate, the highest volume fraction is located in region B, near the transition boundary. The different distributions of $T_1$ and $\delta'$ suggest different precipitate responses within the consolidated region. As Jo and Hirano [36] reported, the precipitate sequence of Al-Cu-Li alloys changes with the different ratios between Cu and Li, which can be summarized as follows [36]:

For Cu/Li $> 4$, $\alpha(SSSS) \rightarrow GP\,zones \rightarrow \theta'' \rightarrow \theta'$. (1)

For $2.5 <$ Cu/Li $< 4$, $\alpha(SSSS) \rightarrow GP\,zones + \delta' \rightarrow \theta'' + \theta' + \delta' \rightarrow \delta' + T_1 \rightarrow T_1$. (2)

For $1 <$ Cu/Li $< 2.5$, $\alpha(SSSS) \rightarrow GP\,zones + \delta' \rightarrow \theta' + \delta' \rightarrow \delta' + T_1 \rightarrow T_1$. (3)

For Cu/Li $< 1$, $\alpha(SSSS) \rightarrow \delta' + T_1 \rightarrow T_1$. (4)

Therefore, the Cu content measured from EDX, with the volume fraction of precipitates along a horizontal line (within the boundary of

the inward material flow), is summarized in Fig. 8(c). Instead of forming a complete *SSSS*, Cu is pushed by the material flow to the transition boundary and agglomerates, resulting in a spike of Cu content located around x = 2 mm. The $T_1$ precipitate volume fraction mainly follows the Cu content. In this regard, the Li concentration is higher at the position where the $T_1$ precipitate volume fraction is low, promoting the precipitation of $\delta'$. Li is considered to be completely dissolved based on the phase diagram for the current composition (AlCu6Li2). Therefore, after subtracting the $T_1$ precipitate volume fraction, the Cu/Li ratio at positions A1 and B1 is 0.68 and 1.03, respectively, indicating different precipitate responses.

The dimensions of the precipitates were examined via bright-field scanning transmission electron microscope (BF-STEM), see Fig. 9. The $T_1$ precipitate exhibits a thin plate morphology with a hexagonal structure on {111} planes of the Al-matrix, with an orientation relationship of $(0001)_{T_1}//\{111\}_{Al}$, $\langle 10\overline{1}0\rangle_{T_1}//\langle 110\rangle_{Al}$, resulting in four variants. Similarly, $\theta'$ precipitates also form thin plates on {100} planes of the Al-matrix, with an orientation relationship of $(001)_{\theta'}//(001)_{Al}$, $[100]_{\theta'}//[100]_{Al}$, which provides three variants [8,37]. Due to their specific habit planes, the observed grain is usually oriented along specific zone axes, i.e. $<110>_{Al}$ for $T_1$ and $<001>_{Al}$ for $\theta'$, where a maximum of two variants will appear edge-on, forming line features with angles of 70.53° and 90°, respectively. Due to the physical constraint of TEM imaging, accessing the aligned crystal axes in multiple samples is non-trivial. As a result, the $<112>_{Al}$ zone axis is also commonly utilized in the literature for imaging $T_1$ precipitates [38], revealing only one variant, see Fig. 8(b). It is important to note that a direct comparison of precipitate density from images acquired along different incident beam axes is not appropriate, as the area density of $T_1$ observed along <110> zone axis is approximately twice that observed along <112> . In Figs. 9(a) and (c), the observing orientation was along $<110>_{Al}$ zone axis and angles between the line features are measured at 69.2° and 71.4°, respectively, confirming the identification of the precipitates as $T_1$. The average diameter of $T_1$ before and after artificial aging is approximately 121 ± 37 and 147 ± 67 nm, respectively and the thickness of $T_1$ is approximately 2.2 ± 1 nm after artificial aging, resulting in an aspect ratio of more than 50, which aligns with the plate morphology reported in the literature. Surprisingly, the thickness of the $T_1$ (~10 nm) is much larger in the as-FCed state, which is reported mainly at the grain boundary in the literature [35]. The volume fraction approximated from the BF-STEM images is 0.02 at A1 in the FCed state and 0.035 for regions A1 and B1 in the artificially aged samples, see Fig. 9(a) and (c). The $\delta'$ precipitate, with a spherical morphology and a diameter of approximately 5 nm, was also found, see Fig. 9(c) (inset). Additionally, a $\theta'$ precipitate was observed, Fig. 9(c), which was not detected in HEXRD, suggesting that its quantity is minimal and does not significantly contribute to the strength of the material.

### 3.3. Mechanical properties

#### 3.3.1. Microhardness

Fig. 10 presents the microhardness distributions of the 20 s as-FCed and artificially aged samples. The consolidated region can be identified by microhardness values exceeding 80 $HV_{0.2}$. In the as-FCed sample, a bowl-shaped feature adjacent to the rotational axis is observed, with a morphology closely resembling the microstructural features, suggesting a strong correlation between them. According to the previous findings in the microstructural investigation, this boundary formation is attributed to the inward material flow introduced by the scroll feature of the die. A different hardness distribution emerges in the artificially aged sample, which closely follows the corresponding precipitation distribution, see Fig. 8. Compared to the peak-aged microhardness values reported for commercial AA2198 Al-Cu-Li alloys under similar aging conditions [38,39], the higher microhardness observed in the FCed sample already suggests that FC is a promising route for fabricating high-strength Al-Cu-Li alloys. The following discussion section will further explore the correlation between mechanical properties and the precipitation strengthening effect.

#### 3.3.2. Microflat tensile testing

The comparison of yield strength (YS), ultimate tensile strength (UTS), and elongation between the 20 s as-FCed and artificially aged samples, obtained via microflat tensile testing, is summarized in Table 1. After artificial aging, the average YS increased from 220 MPa to 275 MPa, and the UTS increased from 345 MPa to 370 MPa, while elongation decreased from 14 % to 8 %. This phenomenon reflects the well-known strength-ductility dilemma from common strengthening strategies [40]. Although the feedstock material (AlCu6Li2) was processed directly from

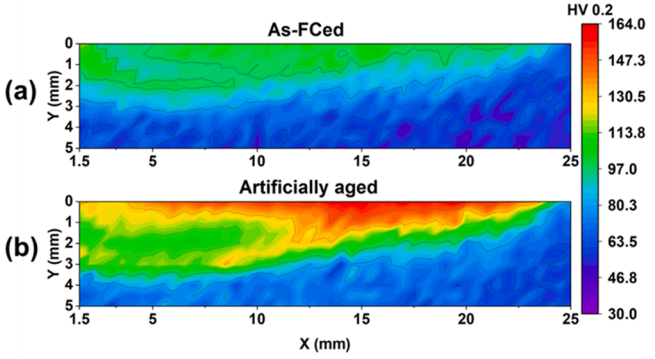


**Fig. 10.** Microhardness distribution in the cross section of the 20 s sample in the as-FCed state (a) and artificially aged at 175 °C with 20 h (b).

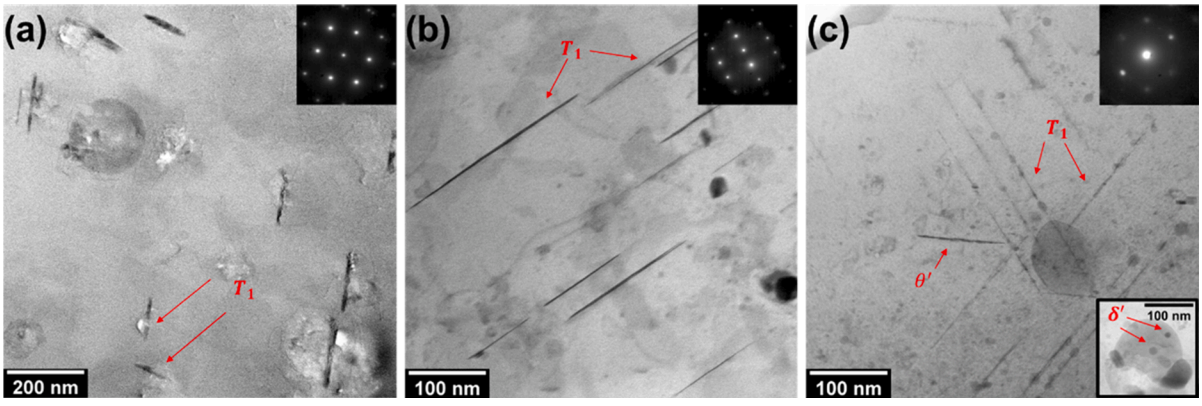


**Fig. 9.** BF-STEM images located at position A1 in the as-FCed state (a) and in the artificially aged state (b) as well as position B1 in artificially aged state (c), with the corresponding imaging orientation along $<110>_{Al}$, $<112>_{Al}$ and $<110>_{Al}$, respectively.

**Table 1**
Yield strength, ultimate tensile strength and elongation at three different positions in the 20 s as-FCed and artificially aged samples.

| | As-FC group 1 | As-FC group 2 | As-FC group 3 | Aged group 1 | Aged group 2 | Aged group 3 |
|---|---|---|---|---|---|---|
| **Yield strength [MPa]** | 221.6 (±12.76) | 213.8 (±3.90) | 225.4 (±22.18) | 245.3 (±2.79) | 306.7 (±4.25) | 274.2 (±2.32) |
| **Ultimate tensile strength [MPa]** | 345.2 (±12.00) | 339.7 (±2.37) | 350.5 (±12.44) | 357.8 (±2.32) | 388.2 (±5.25) | 364.3 (±3.16) |
| **Elongation [%]** | 10.9 (±1.40) | 16.3 (±1.16) | 15.4 (±2.85) | 8.7 (±1.95) | 6.5 (±1.60) | 10.2 (±1.40) |

powder and without additional alloying elements, the YS and UTS are only slightly lower (~85 %) than those of similar commercial Al-Cu-Li alloys, such as AA2198, processed by other friction stir-based methods [39,41], indicating the potential of FC to support novel alloy design.

Inhomogeneous properties were observed across different testing regions. In the as-FCed sample, tensile testing groups 1 and 3 exhibited more scattering, indicating inhomogeneity in the direction parallel to the plunge direction of the FC die, a phenomenon also discussed in literature [18,21]. In contrast, group 2, taken from the interface, showed more homogeneous properties since such a gradient is not present. Such inhomogeneity was mitigated after artificial aging; however, a new form of inhomogeneity emerged. Specifically, the increase in YS varied across groups 1, 2, and 3 by 23.7 MPa, 88.9 MPa, and 48.2 MPa, respectively. This variation is attributed to the $T_1$ and $\delta'$ precipitates, which have distinct distributions across the testing regions, see Fig. 8. The correlation between precipitate distribution and the observed YS increase is of particular interest and deserves further quantitative investigation, which will be detailed in the following section.

## 4. Discussion

### 4.1. Microstructure evolution

The grain structure evolution of powders from the compacted blended state to the consolidated region has been reported to progress through several stages [17,27,28]. Initially, away from the die-feedstock interface, the compacted blended powder exhibits a high density of voids, indicating that compaction alone is insufficient to completely diminish the voids. As the region approaches the die-feedstock interface, slightly elevated temperatures begin to soften the powder, while moderate compressive strain facilitates the gradual elimination of voids. However, alloying is not yet observed at this stage due to the limited shear strain. Typically, a tortuous region is subsequently identified, characterized by non-uniform material flow. This region exhibits high shear deformation and higher temperatures, combined with close contact between powder particles, facilitating the initiation of mechanical alloying. The tortuous region becomes more prominent when the mixed powder has distinct strengths, such as a mixture of Cu and Nb with a 1:1 mass ratio [42]. In the current study, AlCu powder dominates the powder mixture, therefore, the torturous region is likely minimized and not evident. Near the die-feedstock interface, the highest temperature as well as the highest shear stain result in significant grain refinement through dynamic recrystallization [17].

### 4.2. Precipitate evolution

Al-Cu-Li alloys are well known as precipitation hardenable alloys. Before delving into the strengthening effects of each precipitate, it is crucial to understand the formation mechanisms behind the distinct precipitation distributions observed in this study. The experimental alloy composition was designed to highlight mechanical alloying via friction consolidation (FC), containing only the primary ternary elements of Al, Cu, and Li, which is rarely reported. However, the precipitation behavior in Al-Cu-Li alloys has been extensively studied, including friction-based processing methods like Friction Stir Welding and Processing (FSW/P). Before comparing the findings from FSW/P with FC, it is essential to highlight the differences between these two processes as summarized in supplementary table S1. One critical difference is the translational movement of the non-consumable tool. In FSW, the translational movement shifts the heat source constantly throughout the process, whereas in FC, the heat source remains quasi stationary. This fundamental difference influences the thermal history such as the duration of high temperature exposure and the subsequent cooling rate, which affects the microstructure with regards to the grain size and the precipitates [43–45]. For instance, grain growth has been reported at the top of the consolidated region in FC due to prolonged high temperature exposure [21]. Consequently, at similar heat input, finer grains are expected in FSW, enhancing the Hall-Petch strengthening effect. Nevertheless, in precipitation hardenable alloys, mechanical properties are governed more by precipitation hardening rather than by Hall-Petch strengthening. Hence, the following discussion focuses on precipitate evolution and its influence on mechanical properties.

In friction-based processes, different precipitates form in various zones, including the stir zone (SZ), thermo-mechanically affected zone (TMAZ), heat-affected zone (HAZ), and BM. Two different precipitate types have been reported in the FSWed AA2195-T8 SZ: (1) $T_B$ phase, occasionally accompanied by additional $\delta'/\beta'$ and GP zones, along with the partial or complete dissolution of $T_1$ and $\theta'$ precipitates [43,44]; (2) only $\delta'$ phase, with no other precipitates present [45]. The difference between these two precipitate types is attributed to the cooling rates. In the latter case, a thin plate was investigated [45], providing faster cooling that avoids prolonged high-temperature exposure and suppresses the formation of $T_B$ phase, according to the time–temperature-precipitation diagram [46]. Similar complete dissolution of precipitation has also been reported in FSWed AA2050-T8 [47], FSWed AA2060-T8 [48], friction stir processing, and probeless friction stir spot welded AA2198-T8 [49,50] with process temperatures above 450 °C. When the temperature remains below 450 °C, residual $T_1$ precipitates have been found in the SZ, indicating only partial dissolution [47–50]. In the current study on FC, the maximum temperature measured 1 mm behind the die-feedstock interface was 451 °C, as shown in Fig. S1. Given that the heat generation is introduced via the friction between die and feedstock material, the temperature within the FC sample is expected to be higher, suggesting that $T_1$ precipitates should completely dissolve. Although temperature gradients have not been explicitly reported in FC, similar behavior has been described in FE, which is highly similar to FC, but includes an additional extrusion orifice [51]. However, HEXRD and TEM analysis indicate the existence of $T_1$ in the current study. Based on the Al-Cu-Li phase diagram, the nominal composition of AlCu6Li2 contains an Al matrix with $T_1$ phase at 500 °C. Therefore, it can be argued that $T_1$ peaks in HEXRD are mainly from the secondary phases

and the $T_1$ precipitates are formed during cooling [46]. The $T_1$ and $\theta'$ precipitates compete for copper atoms, and $T_1$ is observed to preferentially precipitate over $\theta'$ due to its lower formation enthalpy [52,53]. Besides, the high strain energy introduced by the shear deformation promotes the $\delta'$ phase to precipitate during cooling and natural aging [50,54], consistent with the observed $\delta'$ precipitation after artificial aging.

Since $T_1$ precipitates were not identified in the raw powder using HEXRD, their potential formation mechanisms are worth discussing. $T_1$ nucleation has been widely reported to occur heterogeneously at dislocations, which are associated with the stacking sequence alternation from a face-centered cubic (fcc) to a hexagonal close-packed (hcp) structure [55–57]. Furthermore, Chen et al. [58] proposed that the segregation of Cu around Li-rich particles serves as another nucleation pathway isolated from dislocations. In the present study, dislocations are continuously introduced during FC, combined with the presence of pure Cu in the feedstock, which likely activates both nucleation mechanisms.

The competition in nucleation among various precipitates during artificial aging is of significant interest, as it provides a deeper understanding and strategies for subsequent manipulation of precipitate response. Jo and Hirano [36] proposed that the effect of Cu/Li ratio significantly influences the precipitation sequence in Al-Cu-Li alloys. Since then, this principle has been widely adopted to predict the precipitation behavior. In alloys with a low Cu/Li ratio (1–4), the precipitation of $\delta'$ and $T_1$ is promoted, while the formation of $\theta'$ is suppressed. When Cu/Li ratio drops below 1, $\theta'$ precipitation is completely hindered, and an acceleration of $\delta'$ precipitates is expected. These predictions align well with the HEXRD and TEM observation, although with a small amount of $\theta'$ precipitates presence in position B1, see Fig. 9(c). The nucleation of a new precipitate simultaneously creates a new interface with the matrix, which can be classified into three types based on lattice mismatch, namely coherent, semi-coherent, and incoherent interfaces. Coherent interfaces exhibit minimal lattice mismatch and low interfacial energy; semi-coherent interfaces exhibit medium lattice mismatch and medium interfacial energy; and incoherent interfaces exhibit large lattice mismatch and high interfacial energy. The $\delta'$ precipitate is coherent with the Al matrix, possessing an $L1_2$ structure with a very small lattice mismatch (0.08 %) and low interfacial energy (0.014 $Jm^{-2}$) [59,60]. Meanwhile, $T_1$ precipitate is coherent along $(0001)_{T_1}//\{111\}_{Al}$ but semi-coherent on other planes. Consequently, the $T_1$ precipitate shows a thin plate morphology with a large coherent interface area to minimize its total interfacial energy [53]. The $T_1$ precipitate is generally identified as semi-coherent with the Al matrix, showing a moderate lattice mismatch (0.12 %) and a higher interfacial energy ($0.13-0.23\ Jm^{-2}$) [54,61]. To overcome the higher energy barrier for $T_1$ nucleation, $T_1$ preferentially nucleates at higher energy sites such as dislocations, grain boundaries, and subgrain boundaries. In contrast, $\delta'$ precipitates nucleate more readily within the grain interior.

### 4.3. Precipitate strengthening effect

Researchers [62–67] have been attempting to estimate the strengthening effects of the precipitate via various models, which mainly require the dimensions and the volume fraction of the precipitates as well as other properties, such as antiphase boundary energy, shear modules and Burgers vector. Order strengthening is reported as the most effective strengthening effect of the $\delta'$ precipitate, which creates an antiphase boundary by shearing the ordered precipitate on its slip plane. The theoretical critical resolved shear stress (CRSS) for order strengthening is described as [62]:

$$\Delta\tau_{OH} = \frac{\gamma_{apb}}{2b}\left[\left(\sqrt{\frac{3\pi^2\gamma_{apb}f_{v1}r_0}{32Gb^2}}\right) - f_v\right], \tag{5}$$

where $\gamma_{apb} = 0.15\ Jm^{-2}$ is the antiphase boundary energy for Al, $G = 30\ GNm^{-2}$ is the shear modulus, $b = 0.2864\ nm$ is the Burgers vector, $r_0$ is the average precipitate radius, and $f_{v1}$ is the volume fraction of the $\delta'$ precipitates. To convert the CRSS into YS, a Taylor factor M ~ 3 is usually applied [63]. The $f_{v1}$ of the $\delta'$ precipitate in groups 1, 2 and 3 are obtained from the Rietveld refinement at the corresponding positions of the microflat tensile specimens and are determined as 0.014, 0.034, and 0.02, respectively. Therefore, the corresponding order strengthening are predicted to be 38, 50 and 43 MPa, respectively.

Early development of the $T_1$ precipitation strengthening models are based on the shear-resistant behavior. Nie et al. [64] utilized the modified Orowan equation based on the rational $T_1$ plate orientation, assuming non-randomly distributed dislocations. Zhu and Starke [65] further developed the relationship between $T_1$ and randomly distributed dislocations, which can be summarized as follows:

$$\Delta\tau_{Orowan} = 0.12G\frac{b}{\sqrt{Dt}}\left(\sqrt{f_{v2}} + 0.7\sqrt{\frac{D}{t}}f_{v2} + 0.12\frac{D}{t}f_{v2}^{3/2}\right)\left\{\ln\frac{0.079D}{b}\right\}, \tag{6}$$

where $D$ and $t$ are the diameter and the thickness of the $T_1$ precipitate, respectively, and $f_{v2}$ is the volume fraction of the $T_1$ precipitates.

However, direct observation of sheared $T_1$ precipitates through high-resolution transmission electron microscopy promoted Nie and Muddle [66] to propose a shear-strengthening model that considers the creation of new precipitate-matrix interfaces during the shearing events. Dorin et al. [67] further included the simultaneously formed stacking fault (SF), which plays an important role in the thickening of the $T_1$ precipitates, as follows:

$$\Delta\tau_{shear} = \frac{1.211D\left[\gamma_i + \left(\frac{t}{2b\cos\varphi\sin\theta} - \frac{1}{2}\gamma_{SF}\right)\right]^{\frac{3}{2}}}{t^2}\sqrt{\frac{bf_{v2}}{\Gamma}}, \tag{7}$$

where $\gamma_i = 0.107\ Jm^{-2}$ and $\gamma_{SF} = 0.005\ Jm^{-2}$ are the interface and SF energy, respectively, $\Gamma$ is dislocation line tension in the Al matrix ~ $Gb^2/2$, $\varphi = 30^\circ$ is the angle between the Burgers vector and <112>, and $\theta = 70.53^\circ$ is the angle between two {111} planes. Although the diameter and thickness threshold for the shearing-to-bypassing transition of $T_1$ precipitate has not been determined, it has been observed that the shearing strengthening model overestimates the effect for larger precipitate ($D > 80$ nm or $t > 1.9$ nm) [57,68]. In the present study, the diameter of $T_1$ precipitate is approximately 121 and 147 nm for as-FCed and artificially aged samples, respectively, as shown in Fig. 9. Therefore, the by-passing mechanism is assumed to be dominant in both cases. The $f_{v2}$ of the $T_1$ precipitate obtaining from Rietveld refinement at position A1 in as-FCed sate and at positions A1 and B1 in artificially aged state is equal to 0.03, 0.0376 and 0.045, respectively. The volume fraction obtained from the Rietveld refinement is higher than that observed in TEM. This discrepancy arises because Rietveld refinement characterizes the entire sample without distinguishing between intragranular and intergranular precipitates, a distinction that is relevant in TEM analysis. However, obtaining the distribution of each precipitate from TEM requires extensive work, making the Rietveld refinement a practical alternative for estimating the strengthening contributions of precipitates. Additionally, the precipitate strengthening estimations consider mainly the precipitates within the grains. Therefore, to avoid overestimation, the difference between the as-FCed and artificially aged samples is utilized to visualize the strengthening effect, summarized in Fig. 11. The distribution of the strengthening effect shares similarities to that of the $\delta'$ distribution and microhardness observed after artificial aging, see Fig. 8(b) and Fig. 10(b), suggesting that the primary strengthening effect in the current sample during artificial aging is due to $\delta'$. Several studies attempt to further increase the mechanical

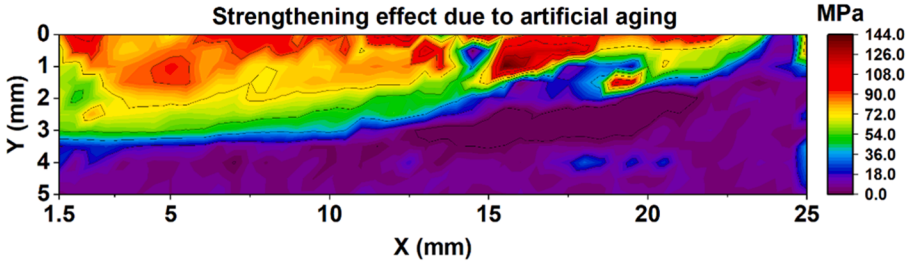


**Fig. 11.** Strengthening effect due to artificial aging from $\delta'$ and $T_1$ compared to as-FCed state.

properties of Al-Cu-Li alloys by modifying the artificial aging procedure, i.e. introducing pre-deformation or two-stage aging, to suppress the formation of intergranular $T_1$ and establish more heterogeneous nucleation sites for intragranular $T_1$ formation, preventing the condition to initiate tensile cracks propagation [69]. This suggests the potential to further improve the strengthening effect. However, the optimization of the subsequent artificial aging analysis is out of the scope of the present study.

## 5. Conclusions

In the present study, an Al-Cu-Li alloy is successfully manufactured via friction consolidation (FC) from different powders. The mechanical alloying effect through FC is characterized in terms of phase transformation behavior, and the corresponding mechanical properties are investigated. The main conclusions are drawn as follows:

(1) The mechanical alloying effect of the AlCu6Li2 alloy through FC from raw powder demonstrates the viability of FC as a potential and energy efficient technique for aluminum alloy design.
(2) The evolution of material flow introduced by the die during FC can be separated into two main subcategories: (a) the inward flow introduced by the scroll-die feature and (b) the downward flow associated with slight shear deformation, which compensates for the additional material drawn by the inward material flow. As processing time increases, the inward flow gradually replaces the downward flow, indicating the expansion of the recrystallization region.
(3) The microhardness and tensile testing results exhibit comparable mechanical properties to other friction stir-based processes. The further enhancement of mechanical properties after subsequent artificial aging treatment indicates the formation of a supersaturated solid solution (*SSSS*), which further confirms the mechanical alloying effect introduced by FC.
(4) The distribution of $T_1$ precipitates after the FC process has a strong relationship with shear deformation. With the differing consumption of Cu and Li during the formation of $T_1$ precipitates, a distinct distribution of $\delta'$ has been observed after artificial aging, which has been identified as the predominant strengthening phase after artificial aging in the present study.

The demonstrated mechanical alloying capability of FC using various powder feedstocks enables novel alloy design. Beyond enabling minor alloying from a classical alloying approach, FC facilitates the development of alloys under non-equilibrium conditions due to its solid state nature, which is unattainable through melting. One application is to systematically increase the Li content to investigate the increase solubility of the Li in the Al matrix. Additionally, the energy-efficient and time-effective FC accelerates the alloy development time with potentially decreased energy consumption. The insights gained from FC can be further extrapolated to other friction stir based technologies, e.g., friction stir processing, to modify the local alloy composition.

## CRediT authorship contribution statement

**Chang Yin-Cheng Chan:** Writing – review & editing, Writing – original draft, Visualization, Methodology, Investigation, Formal analysis, Data curation, Conceptualization. **Uceu F.H.R. Suhuddin:** Writing – review & editing, Visualization, Supervision, Resources, Project administration, Methodology, Investigation, Conceptualization. **Emad Maawad:** Writing – review & editing, Resources, Investigation, Data curation. **Mark T. Mordridge:** Writing – review & editing, Resources, Investigation, Data curation. **Benjamin Klusemann:** Writing – review & editing, Supervision, Resources, Project administration, Funding acquisition, Conceptualization.

## Declaration of competing interest

The authors declare that they have no known competing financial interests or personal relationships that could have appeared to influence the work reported in this paper.

## Acknowledgments

This project has received funding from the European Research Council (ERC) under the European Union's Horizon 2020 research and innovation programme (grant agreement No 101001567). We acknowledge DESY (Hamburg, Germany), a member of the Helmholtz Association HGF, for the provision of experimental facilities. Parts of this research were carried out at P07 beamline of PETRA III and we would like to thank Dr. Norbert Schell for his assistance. The authors also acknowledge Ms. Ana Rodrigues Cameirão from the Institute of Material and Process Design (Helmholtz-Zentrum Hereon) for the experimental assistance.

## Appendix A. Supplementary data

Supplementary data to this article can be found online at https://doi.org/10.1016/j.matdes.2025.114847.

## Data availability

The data related to this research is published online under https://doi.org/10.5281/zenodo.13756860.

## References

[1] R.J. Rioja, J. Liu, The evolution of Al-Li base products for aerospace and space applications, Metall. Mater. Trans. A 43 (2012) 3325–3337, https://doi.org/10.1007/s11661-012-1155-z.
[2] R.J.H. Wanhill, G.H. Bray, Aerostructural design and its application to aluminum–lithium alloys, in: N.E. Prasad, A.A. Gokhale, R.J.H. Wanhill (Eds.), Aluminum–lithium Alloys, Butterworth-Heinemann, 2014, pp. 27–58, https://doi.org/10.1016/B978-0-12-401698-9.00002-1.
[3] A.A. El-Aty, Y. Xu, X. Guo, S.H. Zhang, Y. Ma, D. Chen, Strengthening mechanisms, deformation behavior, and anisotropic mechanical properties of Al-Li alloys: a review, J. Adv. Res. 10 (2018) 49–67, https://doi.org/10.1016/j.jare.2017.12.004.
[4] T. Dorin, F. De Geuser, W. Lefebvre, C. Sigli, A. Deschamps, Strengthening mechanisms of T1 precipitates and their influence on the plasticity of an Al–Cu–Li

alloy, Mater. Sci. Eng. A 605 (2014) 119–126, https://doi.org/10.1016/j.msea.2014.03.024.
[5] B. Jiang, F. Cao, H. Wang, D. Yi, Y. Jiang, F. Shen, B. Wang, H. Liu, Effect of aging time on the microstructure evolution and mechanical property in an Al-Cu-Li alloy sheet, Mater. Sci. Eng. A 740–741 (2019) 157–164, https://doi.org/10.1016/j.corsci.2020.108759.
[6] R.J. Rioja, Fabrication methods to manufacture isotropic Al-Li alloys and products for space and aerospace applications, Mater. Sci. Eng. A 257 (1) (1998) 100–107, https://doi.org/10.1016/S0921-5093(98)00827-2.
[7] T. Dursun, C. Soutis, Recent developments in advanced aircraft aluminium alloys, Mater. Des. 56 (2014) 862–871, https://doi.org/10.1016/j.matdes.2013.12.002.
[8] Y. Yang, G.A. He, Y. Liu, K. Li, W.K. Wu, C. Huang, Quantitative contribution of T1 phase to the strength of Al-Cu-Li alloys, J. Mater. Sci. 56 (2021) 18368–18390, https://doi.org/10.1007/s10853-021-06432-w.
[9] V. Singh, A.A. Gokhale, Melting and casting of aluminum–lithium alloys, in: N. E. Prasad, A.A. Gokhale, R.J.H. Wanhill (Eds.), Aluminum–lithium Alloys, Butterworth-Heinemann, 2014, pp. 167–185, https://doi.org/10.1016/B978-0-12-401698-9.00006-9.
[10] J. Li, Y. Pan, D. Zhao, S. Lü, S. Wu, W. Guo, Development of a novel high strength and toughness Al–Cu–Li alloy casting billet with a new process, Mater. Sci. Eng. A 854 (2022) 143827, https://doi.org/10.1016/j.msea.2022.143827.
[11] J. Li, Y. Pan, Z. Yan, S. Lü, L. Chen, D. Zhao, W. Guo, S. Wu, Effects of Li content on microstructure evolution and mechanical properties of squeeze-cast Al-5Cu-xLi alloy assisted with ultrasonic treatment, J. Alloys Compd. 961 (2023) 171083, https://doi.org/10.1016/j.jallcom.2023.171083.
[12] D. Liu, B. Yürekli, T. Ullsperger, G. Matthäus, L. Schade, S. Nolte, M. Rettenmayr, Microstructural aspects of additive manufacturing of AlLi alloys with high Li content, Mater. Des. 198 (2021) 109323, https://doi.org/10.1016/j.matdes.2020.109323.
[13] M.A. Munoz-Morris, D.G. Morris, Severe plastic deformation processing of Al–Cu–Li alloy for enhancing strength while maintaining ductility, Scr. Mater. 63 (2010) 304–307, https://doi.org/10.1016/j.scriptamat.2010.04.022.
[14] J. Dong, N. Gao, Y. Chen, L. Cao, H. Song, H. Fröck, B. Milkereit, M.J. Starink, Achieving ultra-high strength of Al-Cu-Li alloys by the combination of high pressure torsion and age-hardening, Mater. Sci. Eng. A 832 (2022) 1425042, https://doi.org/10.1016/j.msea.2021.142504.
[15] Z. Shen, S. Chen, L. Cui, D. Li, X. Liu, W. Hou, H. Chen, Z. Sun, W.Y. Li, Local microstructure evolution and mechanical performance of friction stir additive manufactured 2195 Al-Li alloy, Mater Charact 186 (2022) 111818, https://doi.org/10.1016/j.matchar.2022.111818.
[16] L. Silvestroni, L.M. Rueschhoff, K.A. Acord, R. Castro, C. Powell, Synthesis of far-from-equilibrium materials for extreme environments, MRS Bull. 47 (2022) 1143–1153, https://doi.org/10.1557/s43577-022-00454-8.
[17] X. Li, D. Baffari, A.P. Reynolds, Friction stir consolidation of aluminum machining chips, Int. J. Adv. Manuf. Technol. 94 (2018) 2031–2042, https://doi.org/10.1007/s00170-017-1016-4.
[18] G. Buffa, D. Baffari, G. Ingarao, L. Fratini, Uncovering technological and environmental potentials of aluminum alloy scraps recycling through friction stir consolidation, Int. J. of Precis. Eng. and Manuf.-Green Tech. 7 (2020) 955–964, https://doi.org/10.1007/s40684-019-00159-5.
[19] A. Latif, G. Ingarao, M. Gucciardi, L. Fratini, A novel approach to enhance mechanical properties during recycling of aluminum alloy scrap through friction stir consolidation, J. Adv. Manuf. Technol. 119 (2022) 1989–2005, https://doi.org/10.1007/s00170-021-08346-y.
[20] G. Ingarao, M. Amato, A. Latif, A.D. La Rosa, R. Di Lorenzo, L. Fratini, Life Cycle Assessment of aluminum alloys chips recycling through single and multi-step Friction Stir consolidation processes, J. Manuf. Syst. 68 (2023) 651–659, https://doi.org/10.1016/j.jmsy.2023.05.021.
[21] D. Catalini, D. Kaoumi, A.P. Reynolds, G.J. Grant, Friction consolidation of MA956 powder, J. Nucl. Mater. 442 (1) (2013) S112–S118, https://doi.org/10.1016/j.jnucmat.2012.11.054.
[22] D. Zhang, J.T. Darsell, J. Wang, X. Ma, G.J. Grant, I.E. Anderson, J.R. Rieken, D. J. Edwards, W. Setyawan, T.J. Horn, G.R. Odette, No ball milling needed: alternative ODS steel manufacturing with gas atomization reaction synthesis (GARS) and friction-based processing, J. Nucl. Mater. 566 (2022) 153768, https://doi.org/10.1016/j.jnucmat.2022.153768.
[23] X. Wang, J.T. Darsell, X. Ma, J. Liu, T. Liu, R. Prabhakaran, I.E. Anderson, D. Zhang, Manufacturing ODS steels from GARS powders by friction consolidation and extrusion, JOM 76 (2024) 2899–2913, https://doi.org/10.1007/s11837-024-06584-5.
[24] S. Whalen, S. Jana, D. Catalini, N. Overman, J. Sharp, Friction consolidation processing of n-type bismuth-telluride thermoelectric material, J. Electron. Mater. 45 (2016) 3390–3399, https://doi.org/10.1007/s11664-016-4454-0.
[25] X. Li, H. Das, M. Pole, L. Li, A. Soulami, G.J. Grant, D.R. Herling, M. Efe, Exceptional strength and wear resistance in an AA7075/TiB2 composite fabricated via friction consolidation, Mat. Des. 242 (2024) 113006, https://doi.org/10.1016/j.matdes.2024.113006.
[26] M. Narvan, R.A. Behnagh, N. Shen, M.K.B. Givi, H. Ding, Shear compaction processing of SiC nanoparticles reinforced magnesium composites directly from magnesium chips, J. Manuf. Process. 22 (2016) 39–48, https://doi.org/10.1016/j.jmapro.2016.01.010.
[27] N.R. Overman, M.J. Olszta, M. Bowden, X. Li, A. Rohatgi, S.N. Mathaudhu, G. J. Grant, S.A. Whalen, The onset of alloying in Cu-Ni powders under high-shear consolidation, Mat. Des. 211 (2021) 110151, https://doi.org/10.1016/j.matdes.2021.110151.
[28] M. Komarasamy, X. Li, S.A. Whalen, X. Ma, N. Canfield, M.J. Olszta, T. Varga, A. L. Schemer-Kohrn, A. Yu, N.R. Overman, S.N. Mathaudhu, G.J. Grant, Microstructural evolution in Cu–Nb processed via friction consolidation, J. Mater. Sci. 56 (2021) 12864–12880, https://doi.org/10.1016/j.matchar.2020.110759.
[29] T. Liu, J.D. Leazer, S.K. Menon, L.N. Brewer, Microstructural analysis of gas atomized Al-Cu alloy feedstock powders for cold spray deposition, Surf. Coat. Technol. 350 (2018) 621–632, https://doi.org/10.1016/j.surfcoat.2018.07.006.
[30] A.P. Hammersley, FIT2D: a multi-purpose data reduction, analysis and visualization program, J. Appl. Crystallogr. 49 (2016) 646–652, https://doi.org/10.1107/S1600576716000455.
[31] L. Lutterotti, S. Matthies, H.-R. Wenk, A.S. Schultz, J.W. Richardson, Combined texture and structure analysis of deformed limestone from time-of-flight neutron diffraction spectra, J. Appl. Phys. 81 (1997) 594–600, https://doi.org/10.1063/1.364220.
[32] R.S. Mishra, Z.Y. Ma, Friction stir welding and processing, Mater. Sci. Eng. R. Rep. 50 (2005) 1–78, https://doi.org/10.1016/j.mser.2005.07.001.
[33] X. Li, M. Reza-E-Rabby, A. Guzman, G. Grant, S. Mathaudhu, M. Hinton, A. Reynolds, Strain and strain rate in friction extrusion, J. Mater. Res. Technol. 20 (2022) 882–893, https://doi.org/10.1016/j.jmrt.2022.07.116.
[34] N.E. Prasad, T.R. Ramachandran, Phase Diagrams and phase Reactions in Al–Li Alloys, in: N.E. Prasad, A.A. Gokhale, R.J.H. Wanhill (Eds.), Aluminum–lithium Alloys, Butterworth-Heinemann, 2014, pp. 61–97, https://doi.org/10.1016/B978-0-12-401698-9.00003-3.
[35] S. Duan, Y. Wang, Z. Liu, F. Guo, K. Matsuda, Y. Zou, Multilayer T1 phase precipitated on grain boundary in artificially aged Al–Cu–Li alloy, J. Mater. Res. Technol. 24 (2023) 7782–7787, https://doi.org/10.1016/j.jmrt.2023.05.078.
[36] H.H. Jo, K. Hirano, Precipitation processes in Al-Cu-Li alloy studied by DSC, Mater. Sci. Forum 13 (14) (1987) 377–382, https://doi.org/10.4028/www.scientific.net/MSF.13-14.377.
[37] I. Häusler, C. Schwarze, M. Bilal, D. Ramirez, W. Hetaba, R. Kamachali, B. Skrotzki, Precipitation of T1 and θ′ Phase in Al-4Cu-1Li-0.25Mn During Age Hardening: Microstructural Investigation and Phase-Field Simulation, Materials 10 (2017) 117, https://doi.org/10.3390/ma10020117.
[38] Y. Wang, H. Jiang, X. Wu, Q. Meng, Microstructure and mechanical property evolution of robotic friction stir-welded Al–Li alloys, Crystals 13 (4) (2023) 582, https://doi.org/10.3390/cryst13040582.
[39] K. Lv, C. Zhu, J. Zheng, X. Wang, B. Chen, Precipitation of T1 phase in 2198 Al–Li alloy studied by atomic-resolution HAADF-STEM, J. Mater. Res. 34 (2019) 3535–3544, https://doi.org/10.1557/jmr.2019.136.
[40] Y. Wei, Y. Li, L. Zhu, Y. Liu, X. Lei, G. Wang, Y. Wu, Z. Mi, J. Liu, H. Wang, H. Gao, Evading the strength–ductility trade-off dilemma in steel through gradient hierarchical nanotwins, Nat. Commun. 5 (2014) 3580, https://doi.org/10.1038/ncomms4580.
[41] Y. Tao, D.R. Nia, B.L. Xiao, Z.Y. Ma, W. Wu, R.X. Zhang, Y.S. Zeng, Origin of unusual fracture in stirred zone for friction stir welded 2198-T8 Al-Li alloy joints, Mater. Sci. Eng. A 693 (2017) 1–13, https://doi.org/10.1016/j.msea.2017.03.079.
[42] N.R. Overman, X. Li, M.J. Olszta, E.K. Nickerson, C.T. Overman, S.N. Mathaudhu, G.J. Grant, S.A. Whalen, Microstructural progression of shear-induced mixing in a CuNi alloy, Mater Charact 171 (2021) 110759, https://doi.org/10.1016/j.matchar.2020.110759.
[43] J.A. Schneider, A.C. Nunes, P.S. Chen, G. Steele, TEM study of the FSW nugget in AA2195-T81, J. Mater. Sci. 40 (2005) 4341–4345, https://doi.org/10.1007/s10853-005-2808-8.
[44] R.W. Fonda, J.F. Bingert, Precipitation and grain refinement in a 2195 Al friction stir weld, Metall. Mater. Trans. A 37 (2006) 3593–3604, https://doi.org/10.1007/s11661-006-1054-2.
[45] A.K. Shuklaa, W.A. Baeslack III, Study of microstructural evolution in friction-stir welded thin-sheet Al–Cu–Li alloy using transmission-electron microscopy, Scr. Mater. 56 (2007) 531, https://doi.org/10.1016/j.scriptamat.2006.11.028.
[46] P.S. Chen, B.N. Bhat, Time-temperature-precipitation behavior in Al-Li alloy 2195, NASA/TM 2002–211548 (2002).
[47] F. De Geuser, B. Malard, A. Deschamps, Microstructure mapping of a friction stir welded AA2050 Al–Li–Cu in the T8 state, Phil. Mag. 94 (13) (2014) 1451–1462, https://doi.org/10.1080/14786435.2014.887862.
[48] H. Liu, Y. Hu, C. Dou, D. Sekulic, An effect of the rotation speed on microstructure and mechanical properties of the friction stir welded 2060-T8 Al-Li alloy, Mater Charact 123 (2017) 9–19, https://doi.org/10.1016/j.matchar.2016.11.011.
[49] Z. Zhu, J. Jan, C. Gao, M. Liu, J. Song, Z. Wang, H. Li, Microstructures and mechanical properties of Al-Li 2198-T8 alloys processed by two different severe plastic deformation methods: a comparative study, Mat. Sci. Eng. A 58 (2017) 65–73, https://doi.org/10.1016/j.msea.2016.10.108.
[50] Q. Chu, S. Hao, W. Li, X. Yang, Y. Zou, D. Wu, A. Vairis, On the association between microhardness, corrosion resistance and microstructure of probeless friction stir spot welded Al-Li joint, J. Mater. Res. Technol. 14 (2021) 2394–2405, https://doi.org/10.1016/j.jmrt.2021.07.120.
[51] G. Diyoke, L. Rath, R. Chafle, N. Bem Khalifa, B. Klusemann, Numerical simulation of friction extrusion: process characteristics and material deformation due to friction, Int. J. Mater. Form. 17 (2024) 26, https://doi.org/10.1007/s12289-024-01825-z.
[52] Y. Zhang, J. Ling, H.G. Li, X.Y. Luo, Z.X. Ba, Effect of pre-deformation and artificial aging on fatigue life of 2198 Al-Li alloy, Mater. Res. Express 7 (2020) 046509, https://doi.org/10.1088/2053-1591/ab83a6.
[53] M.P. Agustianingrum, S.K. Verma, D. Petschke, F. Lotter, T.E.M. Staab, S. Tang, L. Cao, N. Zulfikar, H. Cho, T.A. Listyawan, H. Kim, C. Jung, S.-H. Kim, A. Zargaran, K. Kim, Revisiting precipitates in Al-Cu-Li alloys: experiments and

first-principles calculations of thermodynamic stability of Al2CuLi(T1) precipitate, J. Alloy. Compd. 991 (2024), https://doi.org/10.1016/j.jallcom.2024.174495.
[54] Y. Lu, Z.Q. Xu, X.C. Xu, The dynamic evolution of microstructure and mechanical properties of an Al-Cu-Li alloy during multi-axial compression, J. Mater. Sci. Technol. 14 (2021) 2513–2521, https://doi.org/10.1016/j.jmrt.2021.07.106.
[55] J.M. Howe, J. Lee, A.K. Vasudévan, Structure and deformation behavior of T1 precipitate plates in an Al-2Li-1Cu alloy, Metall. Trans. A 19 (12) (1988) 2911–2920, https://doi.org/10.1007/BF02647717.
[56] W.A. Cassada, G.J. Shiflet, E.A. Starke, Mechanism of Al2CuLi (T 1) nucleation and growth, Metall. Trans. A 22 (2) (1991) 287–297, https://doi.org/10.1007/BF02656798.
[57] X.M. Wang, W.Z. Shao, J.T. Jiang, G.A. Li, X.Y. Wang, L. Zhen, Quantitative analysis of the influences of pre-treatments on the microstructure evolution and mechanical properties during artificial ageing of an Al-Cu-Li-Mg-Ag alloy, Mater. Sci. Eng., A 782 139253 (2020), https://doi.org/10.1016/j.msea.2020.139253.
[58] L. Chen, P. Ma, C. Liu, L. Zhan, Z. Zheng, A precipitation pathway of T1 phase via heterogeneous nucleation on Li-rich particle in Al-Cu-Li alloy, J. Alloys Compd. 971 (2024) 172796, https://doi.org/10.1016/j.jallcom.2023.172796.
[59] S.F. Zhang, W.D. Zeng, W.H. Yang, C.L. Shi, H.J. Wang, Ageing response of a Al-Cu-Li 2198 alloy, Mater. Des. 63 (2014) 368–374, https://doi.org/10.1016/j.matdes.2014.04.063.
[60] J. Li, J. Huang, D. Liu, Y. Chen, X. Zhang, P. Ma, Distribution and evolution of aging precipitates in Al-Cu-Li alloy with high Li concentration, Trans. Nonferrous Metals Soc. China 29 (1) (2019) 15–24, https://doi.org/10.1016/S1003-6326(18)64910-6.
[61] S.F. Baumann, D.B. Williams, Experimental observations on the nucleation and growth of δ′ (Al3Li) in dilute Al-Li alloys, Metall. Trans. A 16 (1985) 1203, https://doi.org/10.1007/BF02670325.
[62] A.J. Ardell, Precipitation hardening, Metall. Trans. A 16 (1985) 2131–2165, https://doi.org/10.1007/BF02670416.
[63] H. Ovri, E.A. Jägle, A. Stark, E.T. Lilleodden, Microstructural influences on strengthening in a naturally aged and overaged Al–Cu–Li–Mg based alloy, Mater. Sci. Eng. A 637 (2015) 162–169, https://doi.org/10.1016/j.msea.2015.04.039.
[64] J.F. Nie, B.C. Muddle, I.J. Polmear, The effect of precipitate shape and orientation on dispersion strengthening in high strength aluminum alloys, Mater. Sci. Forum 217–222 (1996) 1257–1262, https://doi.org/10.4028/www.scientific.net/MSF.217-222.1257.
[65] A.W. Zhu, E.A. Strake, Strengthening effect of unshearable particles of finite size: a computer experimental study, Acta Mater. 47 (1999) 3263–3269, https://doi.org/10.1016/S1359-6454(99)00179-2.
[66] J.F. Nie, B.C. Muddle, Microstructural design of high-strength aluminum alloys, J. Phase Equilibria 19 (1998) 543–551, https://doi.org/10.1361/105497198770341734.
[67] T. Dorin, A. Deschamps, F.D. Geuser, C. Sigli, Quantification and modelling of the microstructure/strength relationship by tailoring the morphological parameters of the T1 phase in an Al–Cu–Li alloy, Acta Mater. 75 (2014) 134–146, https://doi.org/10.1016/j.actamat.2014.04.046.
[68] G.J. Zeng, H.R. Li, S.X. Deng, P.C. Ma, Y.L. Chen, T.L. Liu, J.F. Li, D.Y. Liu, G.F. Xu, Detailed investigation on microstructure and strengthening contribution of Al-xCu-1.3Li-X alloy sheets, Mater. Char. 205 (2023) 113278, https://doi.org/10.1016/j.matchar.2023.113278.
[69] H. Feng, Y. Chen, H. Yang, P. Yang, J. Zhang, B. Shu, Effects of aging treatment on the mechanical properties and corrosion resistance of an Al-Cu-Mg-Li alloy, Mater. Today Commun. 35 (2023) 105487, https://doi.org/10.1016/j.mtcomm.2023.105487.